



Decoupled thermal–hydraulic analysis of an air-cooled separated heat pipe for spent fuel pools under natural convection

Hui-Lin Xue¹ · Jian-Jie Cheng¹ · Wei-Hao Ji¹ · Wen-Jin Li¹ · Han-Zhong Tao² · Wei Li¹

Received: 27 October 2022 / Revised: 15 February 2023 / Accepted: 23 March 2023 / Published online: 21 June 2023

© The Author(s), under exclusive licence to China Science Publishing & Media Ltd. (Science Press), Shanghai Institute of Applied Physics, the Chinese Academy of Sciences, Chinese Nuclear Society 2023

Abstract

An investigation of the decoupled thermal–hydraulic analysis of a separated heat pipe spent fuel pool passive cooling system (SFS) is essential for practical engineering applications. Based on the principles of thermal and mass balance, this study decoupled the heat transfer processes in the SFS. In accordance with the decoupling conditions, we modeled the spent fuel pool of the CAP1400 pressurized water reactor in Weihai and used computational fluid dynamics to explore the heat dissipation capacity of the SFS under different air temperatures and wind speeds. The results show that the air-cooled separated heat pipe radiator achieved optimal performance at an air temperature of 10 °C or wind speed of 8 m/s. Fitted equations for the equivalent thermal conductivity of the separated heat pipes with the wind speed and air temperature we obtained according to the thermal resistance network model. This study is instructive for the actual operation of an SFS.

Keywords Decoupled analysis · Separated heat pipe · CAP1400 · Finned tube radiator · Passive cooling

1 Introduction

As conventional energy sources become increasingly exhausted, high-efficiency energy management has become a top priority worldwide [1]. Thus, nuclear power has become pivotal for the transformation of global energy. Compared to traditional fossil fuels, nuclear energy is clean, efficient, economical, and has large-scale stable utilization characteristics. However, nuclear power originates from the energy released by the fission of heavy metal elements, and spent fuel is produced during nuclear reactions. Spent fuel assemblies from existing commercial nuclear power plants are stored in pools. The decay heat of the spent fuel is transferred to the pool and then chilled by an active cooling system that includes pumps, heat exchangers, and water [2]. Figure 1 shows a schematic of the AP1000 spent fuel pool cooling system (SFS) [3], which consists mainly of water pumps, heat exchangers, ion exchangers, and filters.

The SFS primarily cools the pool water through pumps and heat exchangers. However, during a station blackout (SBO) accident, the pumps will not operate, and the water in the spent fuel pool will soon boil. Recent studies have shown that spent fuel will be exposed to the environment within three days, contributing to severe radiation pollution under the event of failure of the active cooling system [4]. Therefore, the concept of passive safety systems has been proposed [5]. Innovative safety systems typically rely on passive safety measures such as natural circulation without an external power drive [6]. Experimental research has substantiated that a passive residual heat removal system can effectively remove the core decay heat under natural convection [7]. A passive cooling system (PCS) has also been demonstrated to improve the safety of nuclear power plants during accidents [8].

Since Grover first introduced heat pipes into nuclear reactors [9], the European Atomic Energy Community has also built reactors chilled with heat pipes [10]. Sviridenko [11] developed a new safety scheme for removing decay heat during emergencies using cryogenic heat pipes. To improve thermal safety during power outages, a vertical, fixed, and coreless heat pipe was proposed as a passive waste heat removal system [12]. The results demonstrate that heat pipes are a viable alternative to PCS for SBO accidents. Ye

✉ Jian-Jie Cheng
cjj-njut@njtech.edu.cn

¹ College of Urban Construction, Nanjing Tech University, Nanjing 211800, China

² School of Energy Science and Engineering, Nanjing Tech University, Nanjing 211800, China

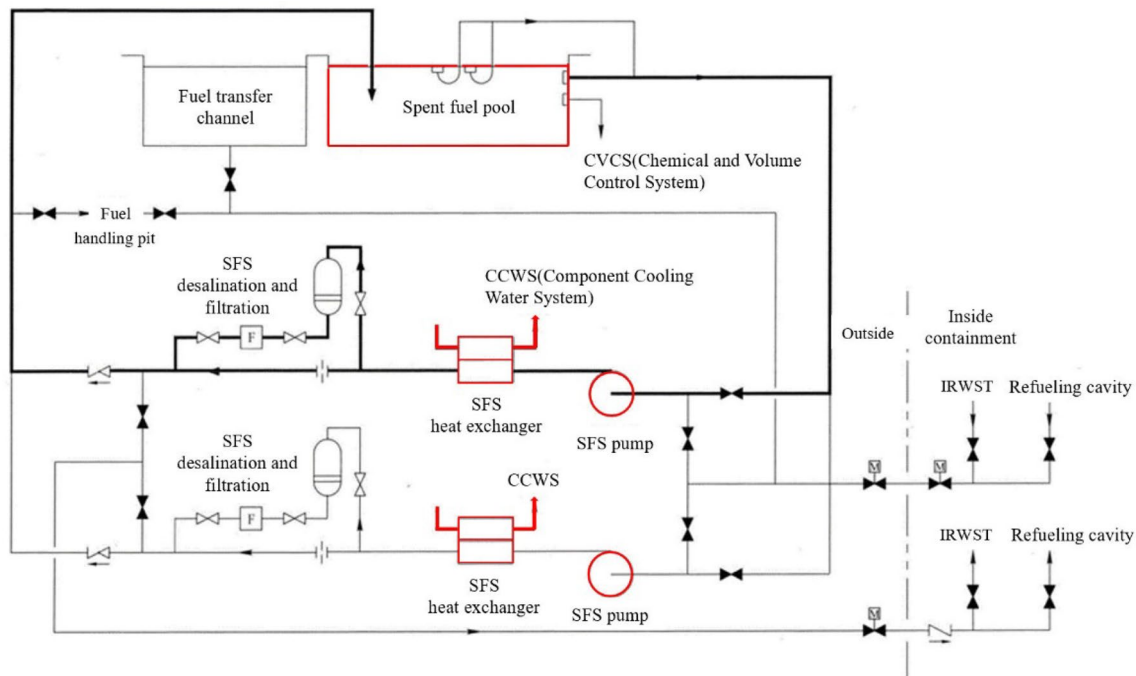


Fig. 1 AP1000 spent fuel pool cooling system

et al. [13] used numerical simulations to study an efficient heat pipe PCS for SBO accidents and proposed the use of collating heat pipe and external air cooling to enhance the cooling capacity of the spent fuel pool (SFP). The system was demonstrated to be effective in removing the decay heat from fuel rods. Wang et al. [14] demonstrated that an air-cooled passive residual heat removal system (PRHRS) was more suitable for long-term cooling by comparing the thermal properties of air and water-cooled PRHRS using the RELAP5/MOD3.4 program. Wang et al. [15] designed a PRHRS that combined water cooling and air cooling with both high cooling and long-term cooling characteristics.

To investigate the convective heat transfer intensity in the pool, Zheng et al. [16] numerically analyzed the temperature and flow field characteristics of an SFP equipped with heat pipes. Bhuiyan and Islam [17] introduced the existing technology and new modes in design-tube heat exchangers under variable flow conditions considering different dispositions and geometric measures. Numerous experimental and numerical studies have explored the transfer characteristics of finned tubes of different diameters, pitches, and heights under natural convection [18–20]. Zhou et al. used computer codes to investigate the effect of the pool temperature on the natural circulation characteristics [21]. Unger et al. and Kumar et al. [22, 23] used numerical simulations to study the effects of the heat pipe bundle structure, tube shape, longitudinal tube spacing, transverse tube spacing, and number of tube rows on the natural

convection heat transfer. Unger et al. [24, 25] experimentally investigated the effects of the tube inclination angle and fin spacing on the natural convection heat transfer in elliptical finned tubes. The empirical results revealed that the heat transfer coefficient increased with the tube inclination angle and fin spacing. Experimental and numerical studies [26, 27] were also conducted on the heat dissipation capability of passive cooling heat pipes in an SFP to explore the effects of the hot water inlet temperature, water flow velocity, and airflow velocity on the heat transfer coefficients of evaporators and condensers.

Previous studies have mainly focused on experimental small-scale separated heat pipes, investigating the entire system or only one part from the perspective of methods and experiments, such as the heat transfer phenomenon of the evaporation segment, hydrodynamic analysis of the riser, or reinforcement of the condensation segment. Currently, the thermal properties of large-scale separated heat pipes in PCS have received less attention because the system involves the coupling of multiple physical processes, such as natural convection between the condenser and air outside the SFP, condensation and evaporation inside the closed circulation of the separated heat pipe, and natural circulation and stratification of the water in the SFP. The air-cooled separated heat pipe radiator is in a state of natural convection in the PCS, which mainly depends on changes in the external environmental parameters. Therefore, it is necessary to decouple the multi-physical heat transfer processes during

operation of the PCS and study the impact of changes in the external environmental conditions on the water temperature of the SFP to ensure safety. Computational fluid dynamics (CFD) techniques have been extensively used in steady-state and transient simulations of nuclear power plant reactors because of their ability to precisely forecast the fluid flow and heat transfer characteristics during 3-D physical phenomena [28]. This has also become a critical technique for decoupling analysis.

In this study, the CAP1400 pressurized water reactor in Weihai City, Shandong Province, was used as the application background, and three-dimensional modeling of the SFP was conducted. ANSYS CFD was used to explore the heat dispersion of the separated heat pipe in the SFS during distinct seasons. Decoupling methods for the three coupled heat transfer processes of the PCS were analyzed to study the effects of air temperature and wind speed on the natural convection of the pool.

2 Numerical methods

2.1 Geometric model

The cooling capacity of the SFP in this study was designed according to 16 MW [29], and the size was taken from the actual parameters of the CAP1400, as listed in Table 1. The separated heat pipe radiator is divided into multiple modules that can be flexibly arranged according to the

actual needs of the system. As shown in Fig. 2a, each side of the SFP extends 2 m outward. Separated heat pipes are mounted around the pool, where the evaporators are inserted. Riser and drop tubes are used to connect the condensation segments outside the pool. The spent fuel is placed at the bottom of the pool. Owing to the temperature dissimilarity between the SFP and the evaporation segments, a natural cycle is formed in the pool with the evaporation segment as the cooling source, spent fuel as the heat source, and water as the heat transfer medium. The condensation segment absorbs heat, such that the internal working medium is vaporized into steam under a pressure difference arising from the temperature in the pool. The steam reaches the condensation segment through the riser pipe, and the liquefied working medium flows back to the evaporation segment due to gravity, forming a closed heat transfer process. We arrange the separated heat pipe condensation segment in ambient air, which creates natural circulation with the condensation segment as the heat source and air as the cooling source.

Figure 2b shows the geometric model of the SFP zone with a single modular separated heat pipes. The condensation segment adopts the form of circular finned tubes to improve the heat transfer efficiency. The evaporation segment is composed of multiple single heat pipes in parallel. Figure 2c shows the geometric model of a single separated heat pipe heat exchanger with a ring fin structure in the condensing section of the heat pipe. Table 1 lists the basic dimensions of the SFP and design parameters of the separated heat pipe.

Table 1 Design parameters of the SFP with separated heat pipes

Parameter	Value
Length of the spent fuel pool, L_{pool} (mm)	11,278
Width of the spent fuel pool, W_{pool} (mm)	5182
Level height of the spent fuel pool, H_{pool} (mm)	12,969
Outer diameter of a heat pipe in the evaporation segment, D_{pipe} (mm)	76
Inner diameter of a heat pipe in the evaporation segment, d_{pipe} (mm)	64
Heat pipe spacing, W_{pipe} (mm)	150
Base tube outer diameter, d_0 (mm)	25
Fin outer diameter, d_f (mm)	50
Fin diameter, d_r (mm)	26
Fin height, H_f (mm)	12
Fin clearance, s_f (mm)	1.4
Tube pitch, s_1 (mm)	54
Average fin thickness, δ	0.4
Number of fins, N_f (piece/m)	434
Number of heat pipes in the evaporation segment, N_v	960
Number of separated heat pipes, N_{hp}	1524
Heat transfer rate of a single module separated heat pipes (including 15 heat pipe radiators), Q_{hp} (W)	105,000
Heat transfer rate of a single heat pipe, Q (W)	7000

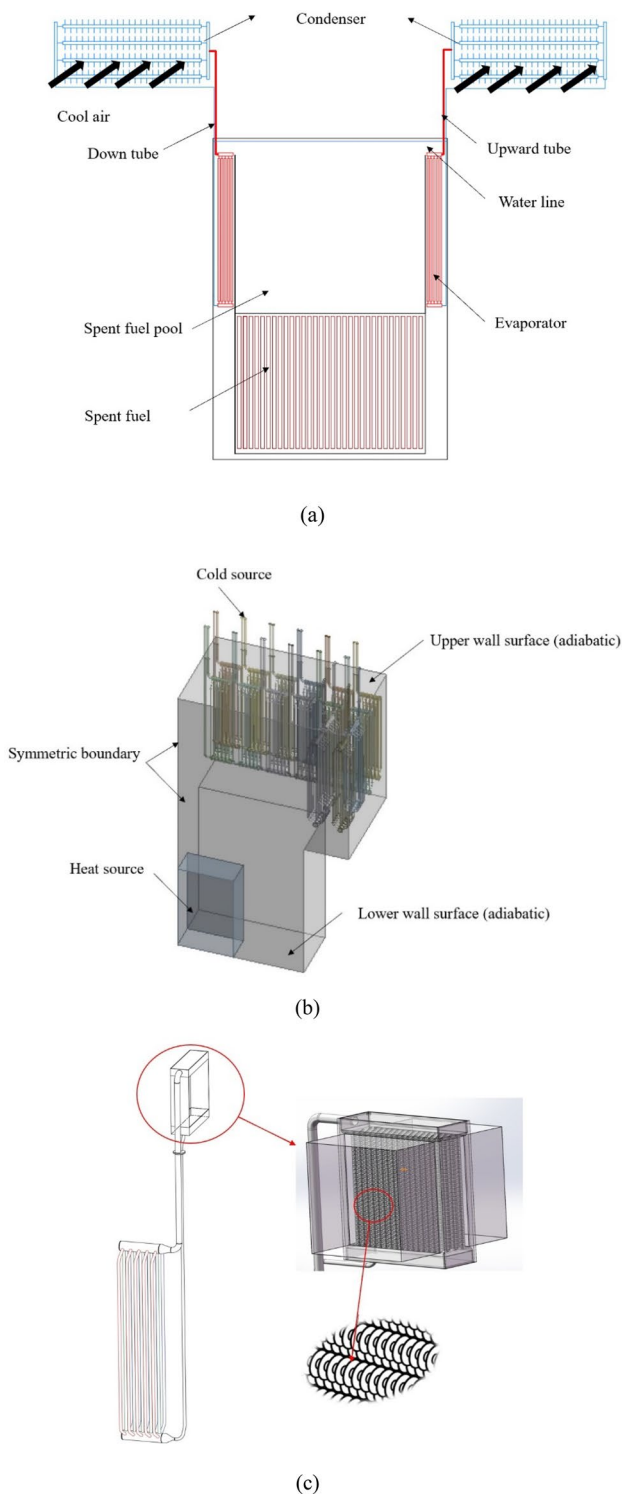


Fig. 2 (Color online) PCS for a spent fuel pool with separated heat pipes: **a** system diagram; **b** numerical model of a single module separated heat pipes with boundary conditions; **c** a separate heat pipe

2.2 Physical model

2.2.1 Design of the condensation section

Compared with plain, corrugated, and spiral finned tubes, ring finned tubes have a stronger heat exchange effect and can adapt to accident working conditions [30]. Therefore, the condensation segment of the separated heat pipe adopts a ring finned tube structure, and the design calculations can be carried out for the air cooler. To obtain the size of the finned tube, we need to estimate the overall heat exchange area and required air volume of the condenser. The heat load is calculated based on condensation of the medium in the tube. Then we assume the total heat transmission coefficient of the condensation segment and estimate the outlet air temperature corresponding to the specific heat formula. Moreover, we need to compute the logarithmic heat transfer temperature difference. Finally, the heat load, total heat transfer coefficient, and heat transfer temperature difference are used to calculate the heat transfer area. Through the above estimation, parameters such as the heat transfer surface area, number of tube bundles, number of tube rows, and air volume of the condenser can be preliminarily determined. The detailed parameters of the condenser structure including the heat transfer and resistance inside and outside the tube bundle can then be calculated. Subsequently an appropriate finned tube form is selected, the relevant parameters in the preliminary design are adjusted, and inspection and verification are conducted [31]. Figure 3 illustrates the specific finned condenser design process, and the required design parameters are listed in Table 2.

2.2.2 Governing equations

Spent fuel is stored at the bottom of the SFP and generates decay heat which is removed by the evaporation segment of the separated heat pipe in the pool. Thus, natural convection driven by temperature differences is created in the SFP. The mass, momentum, and energy control equations [32] are as follows:

$$\frac{\partial \rho}{\partial t} + \nabla(\rho U) = 0, \tag{1}$$

$$\frac{\partial}{\partial t}(\rho U) + \nabla \cdot (\rho U U) = -\nabla p + \nabla \tau + \rho g + F, \tag{2}$$

$$\frac{\partial}{\partial t}(\rho E) + \nabla \cdot (U(\rho E + p)) = \nabla \cdot (k_e \nabla T) + S, \tag{3}$$

where ρ is the density, t is time, U is the spatial velocity vector, τ is the viscous shear stress, $\rho g + F$ is the volume force term, $k_e = \frac{k}{c_p}$ (k is the heat transfer coefficient of the

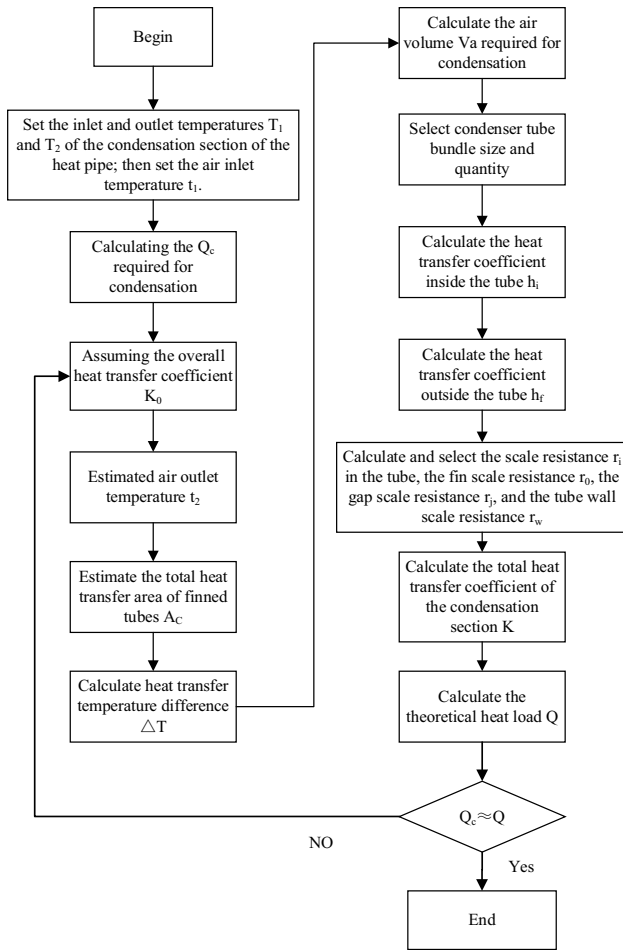


Fig. 3 Design flow chart for the condensation segment

Table 2 Design parameters of the condensation segment

Parameter	Value
Heat transfer rate of a single heat pipe, Q (W)	7000
Total heat transfer area, A_c (m ²)	2.27
Heat transfer coefficient inside the tube, h_i (W/m ² · K)	1423
Heat transfer coefficient outside the tube, h_o (W/m ² · K)	896.4
Intra-pipe scale resistance, R_i (m ² · K/W)	0.00008
Fin scale resistance, R_Σ (m ² · K/W)	–
Contact thermal resistance, R_j (m ² · K/W)	0.00007
Pipe wall fouling thermal resistance, R_w (m ² · K/W)	0.0069
Overall heat transfer coefficient, k_c (W/m ² · K)	110.33

fluid, and c_p is the specific heat capacity of the fluid), S is the internal heat source of the fluid and the portion of the mechanical energy of the fluid converted into internal energy by vicious action, referred to as the viscous dissipation.

Based on the natural convection state in the pool, we define coordinates based on the geometric model and select

the Z axis as the gravitational direction. The $k-\epsilon$ turbulence model is used for the measurement and the turbulence energy generation terms caused by buoyancy are considered when solving the ϵ equation [33].

$$\frac{\partial(\rho k)}{\partial t} + \frac{\partial(\rho k u_i)}{\partial x_i} = \frac{\partial}{\partial x_i} \left[\left(\mu + \frac{\mu_t}{\sigma_k} \right) \frac{\partial k}{\partial x_j} \right] + G_k + G_b - \rho \epsilon, \tag{4}$$

$$\frac{\partial(\rho \epsilon)}{\partial t} + \frac{\partial(\rho \epsilon u_i)}{\partial x_i} = \frac{\partial}{\partial x_i} \left[\left(\mu + \frac{\mu_t}{\sigma_\epsilon} \right) \frac{\partial \epsilon}{\partial x_j} \right] + G_{1\epsilon} \frac{\epsilon}{k} (G_k + G_{3\epsilon} G_b) - G_{2\epsilon} \rho \frac{\epsilon^2}{k}, \tag{5}$$

where G_k is the turbulent kinetic energy generation term due to the average velocity gradient, $G_k = \mu_t \left(\frac{\partial u_i}{\partial x_j} + \frac{\partial u_j}{\partial x_i} \right) \frac{\partial u_i}{\partial x_j}$; G_b is the turbulent kinetic energy generation term due to buoyancy, $G_b = \beta g_i \frac{\mu_t}{Pr_t} \frac{\partial T}{\partial x_i}$; Pr_t is the turbulent Prandtl number, which is $Pr_t = 0.85$ in this model; g_i is the component of gravity acceleration in the i direction; β is the coefficient of thermal expansion, $\beta = -\frac{1}{\rho} \frac{\partial \rho}{\partial T}$; and $C_{3\epsilon} = \tanh \left| \frac{v}{u} \right|$, in which v is the velocity component parallel to the direction of gravity, and u is the velocity component perpendicular to the direction of gravity.

2.2.3 Thermal resistance network model

Typically, thermal resistance network model is used to forecast the heat transfer properties of a heat pipe. A separate heat pipe comprised multiple heat pipes connected in parallel. Thus, the thermal conductivity of each heat pipe is considered to be identical, and the effective thermal conductivity of the heat pipe can be obtained from the total thermal resistance [34]. Figure 4 shows the thermal resistance network model used in this study, ignoring the axial conduction thermal resistance. Table 3 lists the descriptions and calculation formulas for the various thermal resistances of the separated heat pipe, where h is the convective heat transfer coefficient between the fluid and tube wall, A is the convective heat transfer area, the

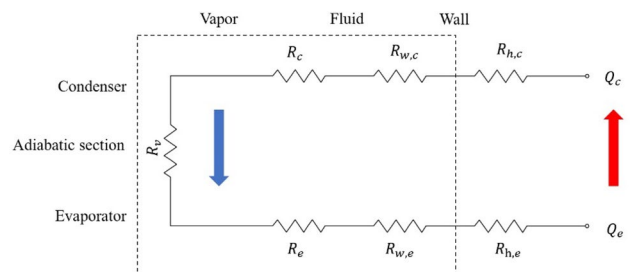


Fig. 4 (Color online) Thermal resistance network model of separated heat pipes

Table 3 Calculation equations for the thermal resistances of separated heat pipes [34]

Thermal resistance	Description and formula
$R_{h,c}$	Convection thermal resistance of the outer wall of the condenser segment $R_{h,c} = \frac{T_{c,out} - T_{c,f}}{Q} = \frac{1}{h_c \cdot A_c}$ $h_c = 0.1378 (\lambda_c / D_c) (\text{Re}_c)^{0.718} \text{Pr}_c^{1/3} (L_c / H_{fin})^{0.296}, \quad \text{Re}_c > 2300$
$R_{w,c}$	Wall conduction thermal resistance of the condenser $R_{w,c} = \frac{T_{c,in} - T_{c,out}}{Q} = \frac{\ln(r_{c,out} / r_{c,in})}{2\pi \lambda_w L_c}$
R_c	Condensation heat resistance of condenser segment $R_c = \frac{T_{sat} - T_o}{Q} = \frac{1}{h_c \cdot \pi \cdot r_{c,in}^2}$ $h_c = 0.943 \left\{ \frac{\rho_l \cdot g \cdot \lambda_l^3 (\rho_l - \rho_v) [h_{fg} + 0.68 c_{p,l} (T_{sat} - T_o)]}{\mu_l L_c (T_{sat} - T_o)} \right\}^{1/4}$
R_v	Vapor flow thermal resistance –
$R_{h,e}$	The convection thermal resistance of the outer wall of the evaporator segment $R_{h,e} = \frac{T_{c,f} - T_{e,out}}{Q} = \frac{1}{h_e \cdot A_e}$ $h_e = 0.11 (\lambda_e / L_e) (\text{Gr}_e \text{Pr}_e)^{1/3}, \quad \text{Gr}_e > 2 \times 10^{10}$
$R_{w,e}$	Convection thermal resistance of the outer wall of the condenser segment $R_{w,e} = \frac{T_{c,out} - T_{e,in}}{Q} = \frac{\ln(r_{e,out} / r_{e,in})}{2\pi \lambda_w L_e}$
R_b	Boiling heat resistance of the evaporation segment $R_b = \frac{T_s - T_{sat}}{Q} = \frac{T_s - T_{sat}}{q^* \cdot \pi \cdot r_{e,in}^2}$ $q^* = \mu_l h_{fg} \left[\frac{g(\rho_l - \rho_v)}{\sigma} \right]^{1/2} \left(\frac{c_{p,l} (T_{sat} - T_o)}{c_{s,l} h_{fg} \text{Pr}_l^2} \right)^3$
R_{tot}	Overall thermal resistance $R_{tot} = R_{h,e} + \left[\sum_{i=1}^n \left(\frac{1}{R_{w,e}} \right)_i \right]^{-1} + \left[\sum_{i=1}^n \left(\frac{1}{R_b} \right)_i \right]^{-1} + R_v + \left[\sum_{j=1}^m \left(\frac{1}{R_c} \right)_j \right]^{-1} + \left[\sum_{j=1}^m \left(\frac{1}{R_{w,c}} \right)_j \right]^{-1} + R_{h,c}$
λ_{eff}	Effective thermal conductivity $\lambda_{eff} = \frac{L_v}{R_{tot} \cdot 2\pi \cdot r^2} (\text{W/m} \cdot \text{K})$

subscripts c, e, l, v are condenser, evaporator, liquid phase, and vapor phase, respectively, D is diameter, λ is equivalent thermal conductivity, H_{fin} is the height of condenser fin, T_{sat} is the saturation temperature of water, $c_{sf} = 0.006$, h_{fg} is specific enthalpy.

2.2.4 Model assumptions and boundary conditions

Before the simulation, the following assumptions were made:

- (1) The wall surface of the pool is adiabatic and the effect of thermal radiation is ignored.
- (2) The thermal conductivity is the same for each separated heat pipe.
- (3) Because the selected model is an intermediate module of the actual model, the walls on both sides of the pool are symmetric.
- (4) A circular section of the drop pipe is used as the cooling source.

- (5) A temperature-dependent fitting function is employed to reflect the change in fluid properties with temperature, and the thermophysical function of water is obtained by fitting the relation of the density, specific heat, viscosity, and thermal conductivity of water at different temperatures.

The thermophysical functions of water are listed in Table 4.

Based on these assumptions, the boundary conditions of the model are shown in Fig. 2b. In this paper, the finite-volume method is selected to obtain the numerical solution. The momentum, energy, and turbulence equations are in the form of second-order upwind discrete functions.

2.3 Decoupling of the three heat transfer processes

Most coupling problems of practical significance cannot be solved analytically; instead, numerical solutions are required. Wang et al. applied porous media to the

Table 4 Thermophysical property functions of the fluid [34]

Parameters	Function expression
Density, ρ (kg/m ³)	$\rho(T) = 231.684 + 6.786T - 0.01886T^2 + 1.579E - 5T^3$
Thermal conductivity, k (J/(kg · K))	$k(T) = -2.297 + 0.0208T - 4.798E - 5T^2 + 3.652E - 8T^3$
Viscosity, ν (W/(m · K))	$\nu(T) = 0.11037 - 9.4075E - 4T + 2.693E - 6T^2 - 2.58E - 9T^3$
Specific heat, c_p (Pa/s)	$c_p(T) = 9025.862 - 40.403T + 0.1096T^2 - 9.62E - 5T^3$

OpenFOAM solver to calculate the coupled heat transfer in shell–and–tube heat exchangers [35]. In addition, RELAP5 is often used to study coupled heat transfer processes in PCS [36, 37]. Gu et al. [38] developed a coupled solution for an Lead/lead–bismuth eutectic (LBE)-cooled reactor using an external loose coupling scheme. This method decomposes the overall model of a pool-type reactor into three models and the output conditions of the former model are the input conditions of the next model. In this study, partition solution and boundary coupling method are used to numerically analyze the heat dissipation characteristics of the separated heat pipe passive cooling system in the SFP. The heat transport in this PCS involves three parts: the SFP, separated heat pipe closed circulation, and atmospheric environment [37].

As shown in Fig. 5a, the condensation segment and atmospheric environment are regarded as region I, the separated heat pipe is regarded as region II, and the evaporation segment and SFP are regarded as region III. Regions I and III both undergo convective heat transfer, while region II experiences coupled heat transfer. This study aims to investigate the influence of varying the parameters in Region I on Region III using a coupled heat transfer process. The decoupling of the three heat transfer processes is the key point of the numerical simulation in this study.

Figure 5b shows a flow chart of the decoupling analysis. First, convective heat transfer occurs between the condenser and the ambient air. We adjust the parameters of the condenser fins and the inlet temperature of the condensing working fluid such that the temperature discrepancy between the inlet and outlet of the condensing working fluid is within 5 °C. The closed loop of the working water in the separated heat pipe loop is then calculated to ensure that the loop pressure drop is zero. Subsequently, the natural circulation in the SFP is calculated such that the lift of the water is identical to its flow resistance. Finally, the heat transmission rate of the system is determined to ensure that the total heat transmission capacity is equal to the 16 MW design value.

The natural circulation of the separated heat pipe loop should satisfy the law of energy conservation. In other words, the heat absorption of the evaporation segment is equivalent to the heat dissipation of the condensation segment, and the pressure drop is zero. The pressure drop of the heat pipe loop can be computed using Eqs. (6) and (7):

$$\Delta P_N = \frac{G_{Ni}^2 + 0.5G_{N2}^2}{2p_i}, \quad (6)$$

$$G_{Ni} = \frac{W_i}{\frac{\pi}{4}d_{Ni}^2}, \quad (7)$$

where G_{Ni} is the mass flow rate of the inlet and outlet, d_{Ni} is the diameter of the inlet and outlet nozzles, and W_i is the mass flow rate of the fluid in the pipe.

The condition for natural circulation of the SFP is that the buoyancy of water is equal to the flow resistance. The total flow resistance of water in the SFP includes the friction pressure loss and local resistance, which can be calculated using Eqs. (8) and (9).

$$\Delta P_{f_w} = \sum_i \left(f_i \times \frac{L_i}{D_i} \times \frac{\rho u_i^2}{2} \right) + \sum_i \left(\xi_i \times \frac{\rho u_i^2}{2} \right), \quad (8)$$

$$f_i = \begin{cases} \frac{64}{Re_i}, & Re_i < 2300 \\ (1.821 \times l_g(Re_i) - 1.64)^{-2}, & Re_i \geq 2300 \end{cases}, \quad (9)$$

where ΔP_{f_w} is pressure loss, f_i is resistance coefficient along the path, ξ_i is local resistance coefficient.

The decoupling is valid if the heat transmission in the condensation segment is equal to that in the evaporation segment. The formulas for heat transmission are given below:

$$Q_c = M \cdot (i_1 - i_2), \quad (10)$$

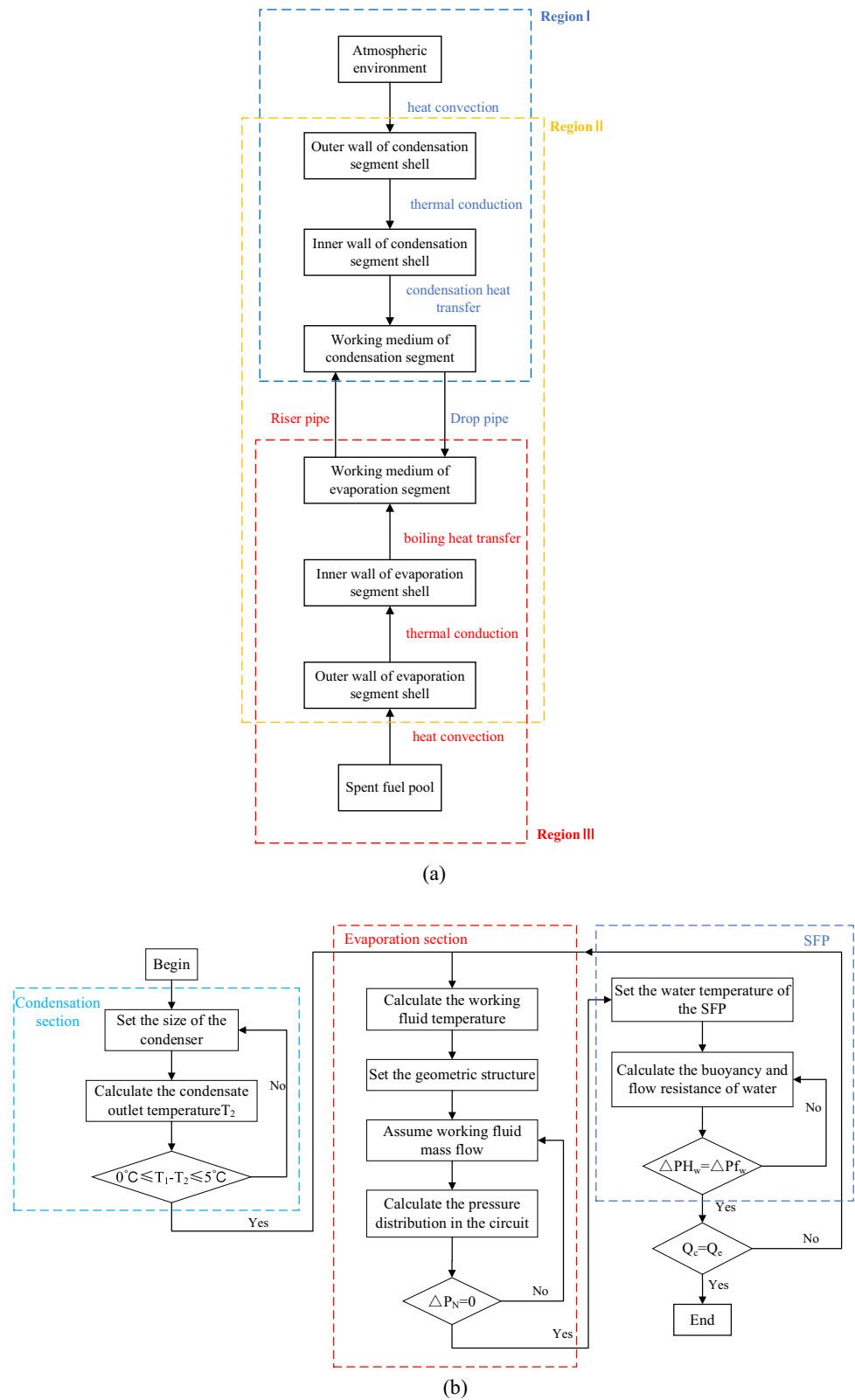
where M denotes the working fluid mass flow rate in the condensation segment, i_1 is the enthalpy of the inlet water vapor, and i_2 is the enthalpy of the outlet condensate.

$$Q_e = A_e \cdot k \cdot (t_{f1} - t_{f2}), \quad (11)$$

$$A_e = \frac{Q}{U_0 \cdot \Delta T}, \quad (12)$$

where A_e is the surface area of the evaporation segment, t_{f1} is the temperature of the working fluid in the heat pipe, t_{f2} is the water temperature in the SFP, ΔT is the average temperature of the heat transfer between the fluid inside and outside the heat pipe, and U_0 is the heat transfer coefficient

Fig. 5 The separated heat pipe of PCS: **a** heat transfer processes; **b** decoupling analysis method



of the evaporation section, which can be referred to as the thermal resistance network model. The power of the heat source used in the numerical calculations is 105 kW.

2.4 Grid independence analysis and model validation

To ensure the accuracy of the numerical simulation, experimental tests were also performed in this study. The test device used in this study represents scale model of the pool. A photograph of the test setup is presented in Fig. 6. The test device includes five sections: an arc heating system, single separated heat pipe radiator, water tank auxiliary heating system, ambient temperature control system, and data acquisition system. The evaporation segment is placed in the pool and the condensation segment is located in the environment. Convective heat transmission in the pool allows heat transfer from evaporation through the riser pipe to the condenser, which dissipates the heat into the air. The condensation segment contains annular fins on the tube bundle and a blower on the upper part. In the tests, the ambient temperature control system provides precise air temperatures, and the arc surface heating system provides different heating powers. A K-type thermocouple is used to measure the temperature at measurement points arranged in separate heat pipes and tanks, and the stability of the test is evaluated by monitoring the temperature changes at each measurement point in the experimental system. Voltage regulators are used to control the power required for each set of trials. During the tests, the output of the portable power regulator is continuously monitored to avoid voltage fluctuations. With this method, we tested the cooling

conditions of the condensation segment under natural and forced convection conditions.

Grid independence analysis is performed to verify that the number of grids is independent of the final flow calculation results and satisfies the accuracy requirements. The meshes near the heat pipe wall surface and heat source are refined. In the grid independence verification, the heat dissipation of the evaporation segment under different schemes is compared. As shown in Fig. 7a, the effect of the grid number on the results can be neglected when the grid number exceeds 2.4×10^6 .

In this study, a separated heat pipe is adopted as the SFP radiator, which is divided into condensation and evaporation segments. Numerical simulations are then performed for these two models. To improve the model validation accuracy, we assume the other walls of the condenser have adiabatic boundary conditions and that the temperature is the same as the environmental temperature in the experiments. For verification, numerical simulations are performed with heating powers of 3, 4, 6, 7.8, and 8 kW. The uncertainty of the heat pipe heat transfer is $\pm 5.2\%$, and the uncertainty of the heat source power is $\pm 1.5\%$ [39]. When the calculation results are stable, the temperatures at the measurement points arranged in the condensation segment are compared with the simulation results. Then, the temperatures at the measurement points at different heights in the pool are selected for comparison with the simulation results. As shown in Fig. 7b and c, the error between the numerical simulation results and the experimental data is within $\pm 10\%$, which meets the model verification requirements.

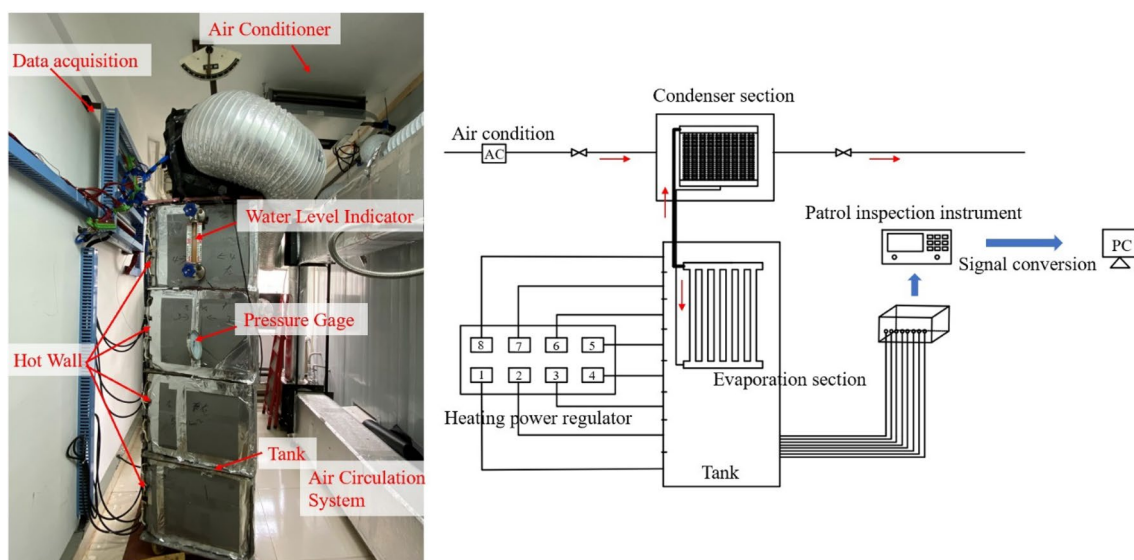
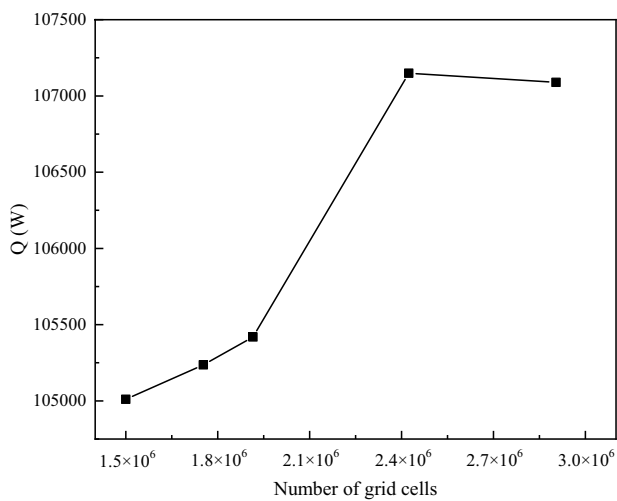
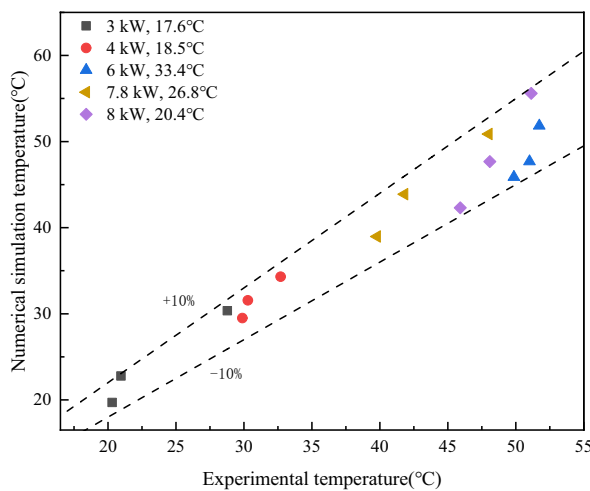


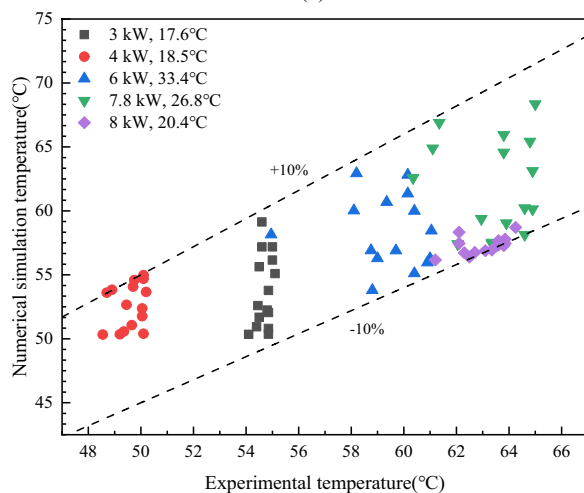
Fig. 6 (Color online) Test device diagram



(a)



(b)



(c)

Fig. 7 (Color online) Numerical model: **a** grid independence test; **b** comparison of simulation results and experimental data in the condenser; **c** comparison of simulation results and experimental data in the pools

3 Results and discussion

3.1 Heat transfer analysis under four seasons climate change

In this study, the SFP heat dissipation unit of an air-cooled heat exchanger is numerically calculated. The thermal properties of the heat sink are analyzed based on the mean temperature of the pool, effective thermal conductivity of the heat pipe, heat dissipation, temperature field, and flow field. Because the temperature distribution of Weihai is consistent, we select the four solar terms of the vernal equinox, summer solstice, autumn equinox, and winter solstice, to reflect the temperature distribution characteristics of the four seasons. Specific data are presented in Table 5.

As shown in Fig. 8, the pool temperature is the highest and heat exchange is the lowest during the summer solstice, while the pool temperature is lowest and heat exchange is highest during the winter solstice. The minimum heat transfer rate reaches 105.384 kW, satisfying the requirements of the single modular heat exchangers (105 kW). As shown in Fig. 9, the water temperature increases gradually with height in areas above 8 m in the pools. At pool heights of

Table 5 Weather conditions and radiation thermal conductivity in Weihai in 2021

Weather	Temperature (K)	Wind speed (m/s)	Effective thermal conductivity (W/m · K)
Vernal equinox	281.15	8	2,249,786
Summer solstice	304.15	5.5	2,076,923
Autumnal equinox	298.15	9	2,282,985
Winter solstice	281.15	10	2,338,814

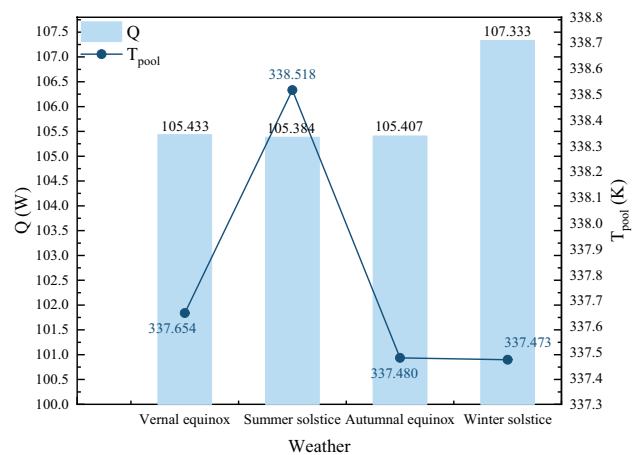


Fig. 8 Comparison of the pool heat exchange and average water temperature in different seasons

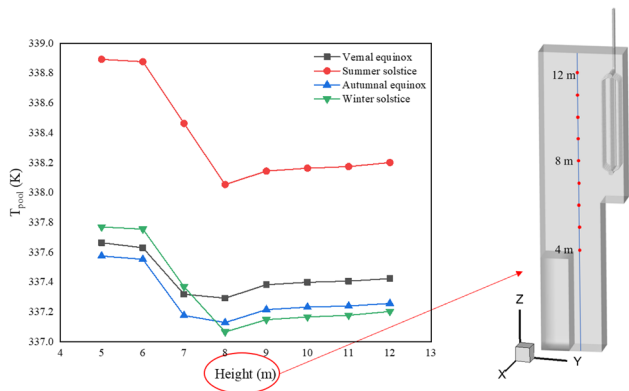


Fig. 9 (Color online) Variation in the average water temperature with height in the XY cross-section in different seasons

0–8 m, the water temperature gradually decreases with the height because the bottom of the pool is closer to the spent fuel.

To clearly visualize the water temperature at different heights and flow field in SFP, we selected a region containing only one separated heat pipe heat exchanger for the cloud analysis. As shown in Fig. 10, the water temperature in the SFP is the highest at the summer solstice, and a significant temperature difference exists between the top and bottom of the SFP. Owing to its buoyancy, the heated fluid rises to the upper part of the pool. Consequently, the temperature at the top of the pool increases slightly, and thermal stratification occurs. In addition, the water temperature on the left side of the pool is lower than that on the right side. Figure 11 shows

Fig. 10 (Color online) Temperature contours of the pool at $z = 4.1$ m, 6.3 m, 8.5 m, and 10.7 m in different seasons: **a** Vernal equinox, **b** Summer solstice, **c** Autumnal equinox, **d** Winter solstice

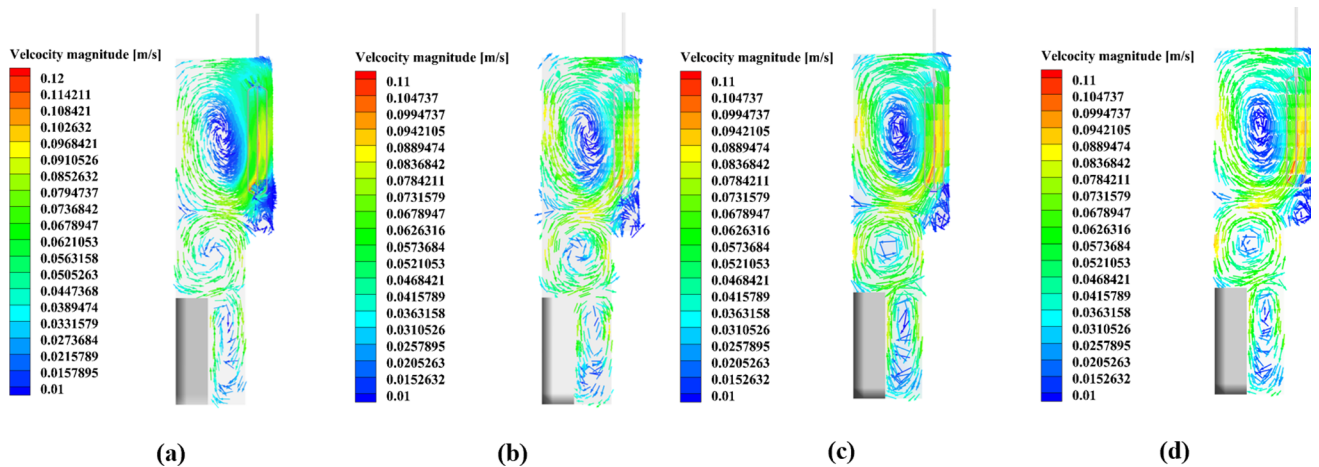
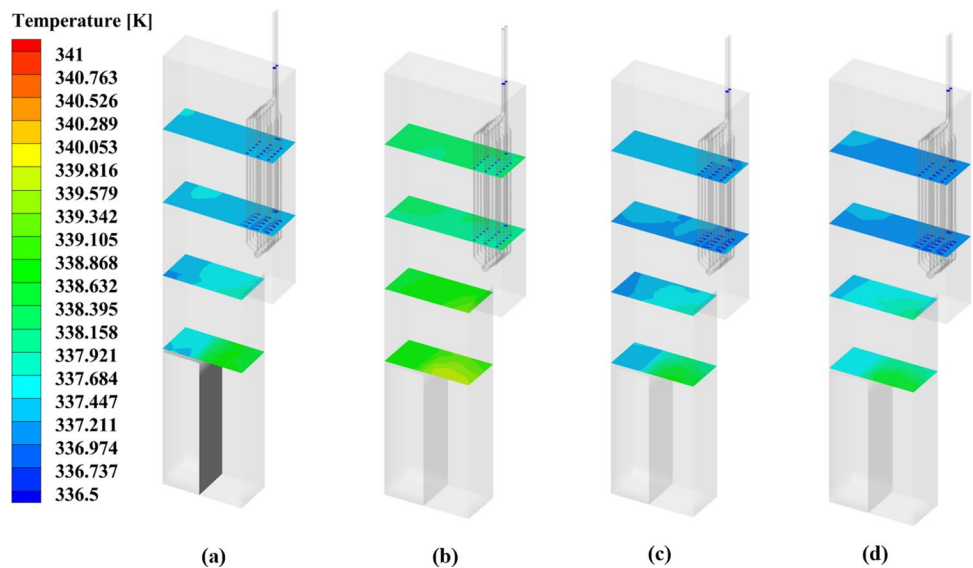


Fig. 11 (Color online) Velocity vector diagram at the ZX section of the SFP: **a** Vernal equinox, **b** Summer solstice, **c** Autumnal equinox, **d** Winter solstice

that the highest velocity in the SFP occurs in the evaporation segment. Three distinct vortex zones are present in the pool, mainly due to the floating force of the natural circulation in the SFP. The water flow at the bottom of the pool rises with a low speed and is distributed in the middle of the SFP owing to buoyancy. Then the water flows along the heat pipe evaporation segment towards the center of the SFP, which causes a temperature discrepancy between the left and right sides of the pool.

3.2 Effects of wind speed

Li et al. [40] used MM5 and CALMET to simulate the distribution of wind energy in Weihai and analyzed the detailed characteristics of the annual average wind energy distribution in different seasons and simulation periods. The simulation results show that the average yearly wind speed in Weihai ranges from 3.3 to 8.8 m/s. Therefore, we choose wind velocity values of 3.5, 4.5, 5.5, 6.5, 7.5, and 8.5 m/s for the numerical analysis; the air temperature is maintained at 30 °C. Thus, we explore the performance characteristics of the SFP radiator under different wind speed conditions.

Based on Table 4, we can calculate the effective thermal conductivity under different wind speed conditions. The calculation results show that the effective thermal conductivity of the heat pipe increases continuously with increasing the wind speed. Therefore, we can obtain the function for the heat conductivity of the heat pipes with wind speed by data fitting, as shown in Fig. 12a:

$$\lambda_{eff} = -9134.3v^2 + 191474.9v + 1298586.024, \quad (13)$$

where λ_{eff} is the effective thermal conductivity of the separated heat pipe, and v is the wind speed. The fitted curve shown in Fig. 12a is in the form of a parabola with a downward opening. When v is 10.48 m/s, λ_{eff} reaches its maximum value. This empirical formula can help improve the prediction of the effect of wind speed on the heat dissipation capacity of PCS. As shown in Fig. 12b, at any cross-sectional height, the higher the wind speed, the lower the average pool temperature will be, which indicates that the heat pipe radiator removes more heat. As shown in Fig. 12c, the temperature of the pool gradually decreases with increasing wind speed, and the maximum temperature difference reaches 2.039 K. In addition, the maximum heat dissipation occurs when v is 8 m/s. In conclusion, when v is 8 m/s, the heat pipe radiator achieves optimal heat transmission performance.

3.3 Effect of air temperature

Wang et al. [41] used a time series model to study the temperature changes in Weihai City, Shandong Province,

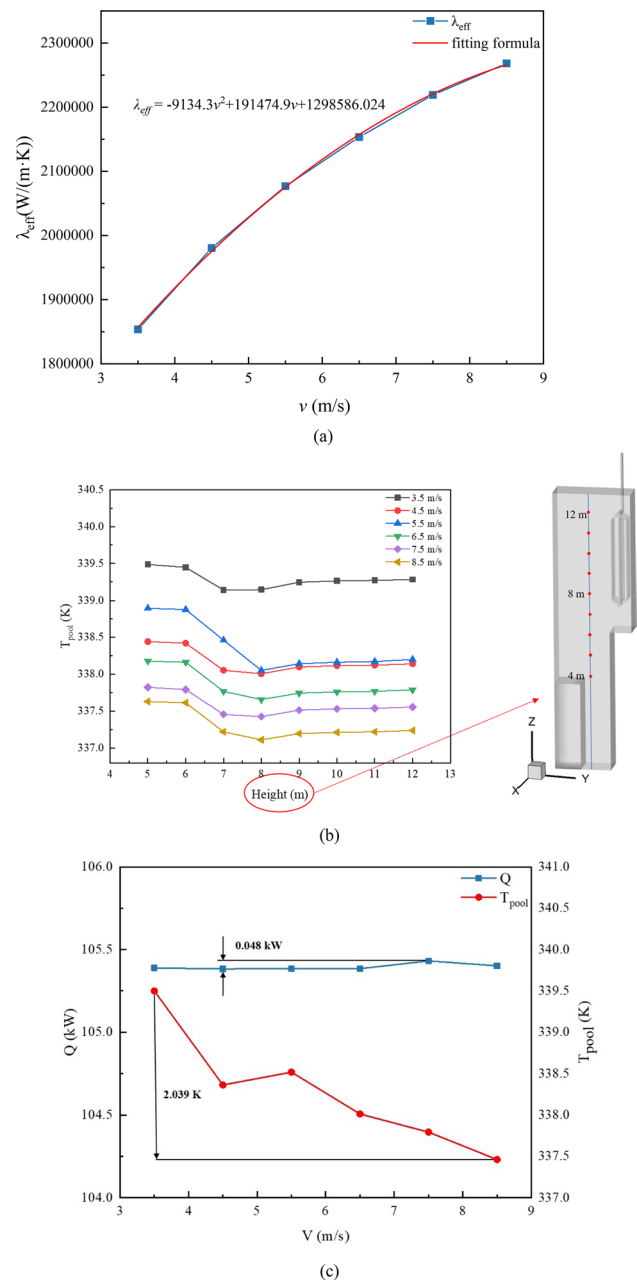


Fig. 12 (Color online) Effect of wind speed: **a** fitting curve for the relationship between the heat pipe thermal conductivity and wind speed; **b** variation in the average temperature of the XY cross-section of the SFP with height; **c** pool heat dissipation and average water temperature

over the past 50 years. Based on the average temperature of each season in the model results, the annual temperature fluctuation range in Weihai in a year is $-3-30$ °C. Thus, we set the wind speed as 5.5 m/s and the air temperature as 5 °C, 10 °C, 15 °C, 20 °C, 25 °C, and 30 °C in the simulation conditions. Thus, we also consider the effect of air temperature on the heat transmission properties of

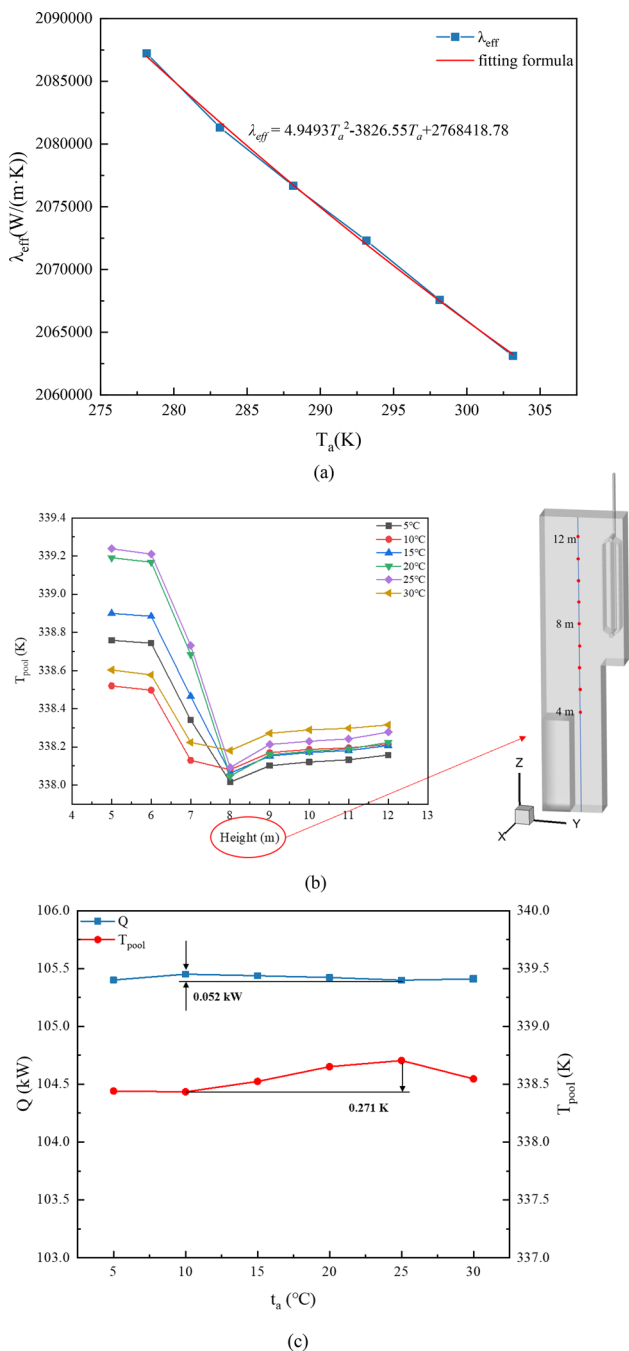


Fig. 13 Effect of air temperature: **a** Fitting curve for the relationship between the heat pipe thermal conductivity and air temperature; **b** Variation in the average temperature of the XY cross-section of the SFP with height; **c** pool heat dissipation and average water temperature

the separated heat pipe radiator and natural convection of the pool.

According to the thermal resistance network model, it can be calculated that λ_{eff} will decrease steadily with increasing air temperature. Therefore, the heat exchange of the PCS will gradually decrease. The data calculated from Table 4

can be fitted to obtain the relationship between the thermal conductivity of the heat pipe and the wind speed as follows:

$$\lambda_{\text{eff}} = 4.9493t_a^2 - 3826.55t_a + 2768418.78, \quad (14)$$

where t_a is the air temperature. Figure 13a shows the fitting curve for the relationship between the thermal conductivity of the heat pipe and the air temperature, which is in the form of a parabola with an upward opening. The lower the air temperature, the higher the thermal conductivity of the separated heat tube heat exchanger will be. This curve has specific reference significance for evaluating the performance of the separated heat pipe radiator under different air temperatures.

As shown in Fig. 13b, when the air temperature is 10–20 °C, the average water temperature variation curves on the XY cross-section almost coincide in the height range of 8–12 m. Under these conditions, the difference in the average temperature of the pool is 0.22 °C, as shown in Fig. 13c. When the air temperature is 10 °C, the temperature of the pool is the minimum, and the heat dissipation of the heat pipe radiator is the maximum. When the air temperature is 10 °C, the heat pipe radiator thus achieves optimal performance.

4 Conclusion

This study used the CAP1400 in Weihai City, Shandong Province, as the application background and conducted three-dimensional modeling of the SFP. We conducted numerical simulations based on the decoupling conditions of the heat transfer process in the SFS. The effects of the air temperature and wind speed on the heat transmission capability of the PCS were investigated using the zonal decoupling method. The specific conclusions are summarized as follows:

- (1) The air-cooled separated heat pipe radiator can satisfy the heat dissipation requirements of the SFP and has better stability in engineering applications.
- (2) The decoupling conditions derived from the partition solution and boundary coupling method are the key to investigating the heat transfer characteristics of the separated heat pipe in the SFS.
- (3) The separated heat pipes can achieve optimal performance when the air temperature is 10 °C or wind speed is about 8 m/s. The wind speed has a more significant impact on the heat dissipation capacity of the separated heat pipe than the air temperature.
- (4) The empirical equations for the thermal conductivity coefficient of the separated heat pipes with respect to changes in wind speed and air temperature can be used to predict the number of air-cooled heat pipe radiators in actual engineering.

Author contributions All authors contributed to the study conception and design. Material preparation, data collection and analysis were performed by Jian-Jie Cheng, Wei-Hao Ji, Wen-Jin Li, Han-Zhong Tao and Wei Li. The first draft of the manuscript was written by Hui-Lin Xue and all authors commented on previous versions of the manuscript. All authors read and approved the final manuscript.

Data availability The data that support the findings of this study are openly available in Science Data Bank at <https://doi.org/10.57760/sciencedb.j00186.00042> and <https://cstr.cn/31253.11.sciencedb.j00186.00042>.

Declarations

Conflict of interest The authors declare that they have no conflict of interest.

References

1. J. Sun, R. Zhang, M. Wang et al., Multi-objective optimization of helical coil steam generator in high temperature gas reactors with genetic algorithm and response surface method. *Energy* **259**, 124976 (2022). <https://doi.org/10.1016/j.energy.2022.124976>
2. S. Unger, M. Arlit, M. Beyer et al., Experimental study on the advective heat flux of a heat exchanger for passive cooling of spent fuel pools by temperature anemometry grid sensor. *Nucl. Eng. Des.* **379**, 111237 (2021). <https://doi.org/10.1016/j.nucengdes.2021.111237>
3. C. Lin, *An Advanced Passive Plant AP1000*. (China, 2008), pp. 275–277
4. J. Wan, H. Lin, Y. Tseng et al., Application of TRACE and CFD in the spent fuel pool of Chinshan nuclear power plant. *Appl. Mech. Mater.* **145**, 78–82 (2011). <https://doi.org/10.4028/www.scientific.net/AMM.145.78>
5. M. Wang, H. Zhao, Y. Zhang et al., Research on the designed emergency passive residual heat removal system during the station blackout scenario for CPR1000. *Ann. Nucl. Energy* **45**, 86–93 (2012). <https://doi.org/10.1016/j.anucene.2012.03.004>
6. M. Wang, D. Zhang, S. Qi et al., Accident analyses for china pressurizer reactor with an innovative conceptual design of passive residual heat removal system. *Nucl. Eng. Des.* **272**, 45–52 (2014). <https://doi.org/10.1016/j.nucengdes.2014.01.019>
7. Z. Xiao, C. Xu, W. Zhuo et al., Steady characteristic investigation on passive residual heat removal system of Chinese advanced PWR. *Nucl. Sci. Tech.* **19**, 58–64 (2008). [https://doi.org/10.1016/S1001-8042\(08\)60023-8](https://doi.org/10.1016/S1001-8042(08)60023-8)
8. M. Wang, A. Manera, V. Petrov et al., Passive decay heat removal system design for the integral inherent safety light water reactor (I2S-LWR). *Ann. Nucl. Energy* **145**, 106987 (2020). <https://doi.org/10.1016/j.anucene.2018.03.014>
9. C. Mueller, P. Tsvetkov, A review of heat-pipe modeling and simulation approaches in nuclear systems design and analysis. *Ann. Nucl. Energy* **160**, 108393 (2021). <https://doi.org/10.1016/j.anucene.2021.108393>
10. Y. Kuang, Q. Yang, W. Wang, Thermal analysis of a heat pipe assisted passive cooling system for spent fuel pools. *Int. J. Refrig.* **135**, 174–188 (2022). <https://doi.org/10.1016/j.ijrefrig.2021.12.021>
11. I.I. Sviridenko, Heat exchangers based on low temperature heat pipes for autonomous emergency WWER cooldown systems. *Appl. Therm. Eng.* **28**, 327–334 (2008). <https://doi.org/10.1016/j.applthermaleng.2006.02.033>
12. M.H. Kusuma, N. Putra, A.R. Antariksawan et al., Passive cooling system in a nuclear spent fuel pool using a vertical straight wickless-heat pipe. *Int. J. Therm. Sci.* **126**, 162–171 (2018). <https://doi.org/10.1016/j.ijthermalsci.2017.12.033>
13. C. Ye, M.G. Zheng, M.L. Wang et al., The design and simulation of a new spent fuel pool passive cooling system. *Ann. Nucl. Energy.* **58**, 124–131 (2013). <https://doi.org/10.1016/j.anucene.2013.03.007>
14. M. Wang, S. Qiu, W. Tian et al., The comparison of designed water-cooled and air-cooled passive residual heat removal system for 300MW nuclear power plant during the feed-water line break scenario. *Ann. Nucl. Energy* **57**, 164–172 (2013). <https://doi.org/10.1016/j.anucene.2013.01.027>
15. Y. Li, P. Song, T. Feng et al., Numerical study on improved design of passive residual heat removal system for China pressurizer reactor. *Nucl. Eng. Des.* **375**, 111087 (2021). <https://doi.org/10.1016/j.nucengdes.2021.111087>
16. W. Zheng, W. Wang, R. Zhuan et al., Analysis of natural convection heat transfer in spent fuel pool cooled with heat pipe. *Atomic Energy Sci. Technol.* **48**, 2250–2256 (2014). <https://doi.org/10.7538/yzk.2014.48.12.2250> (in Chinese)
17. A.A. Bhuiyan, A.K.M.S. Islam, Thermal and hydraulic performance of finned-tube heat exchangers under different flow ranges: a review on modeling and experiment. *Int. J. Heat Mass Transf.* **101**, 38–59 (2016). <https://doi.org/10.1016/j.ijheatmasstransfer.2016.05.022>
18. H.-T. Chen, W.-L. Hsu, Estimation of heat transfer coefficient on the fin of annular-finned tube heat exchangers in natural convection for various fin spacings. *Int. J. Heat Mass Transf.* **50**, 1750–1761 (2007). <https://doi.org/10.1016/j.ijheatmasstransfer.2006.10.021>
19. H.-T. Chen, Y.-S. Lin, P.-C. Chen et al., Numerical and experimental study of natural convection heat transfer characteristics for vertical plate fin and tube heat exchangers with various tube diameters. *Int. J. Heat Mass Transf.* **100**, 320–331 (2016). <https://doi.org/10.1016/j.ijheatmasstransfer.2016.04.039>
20. J.R. Senapati, S.K. Dash, S. Roy, Numerical investigation of natural convection heat transfer over annular finned horizontal cylinder. *Int. J. Heat Mass Transf.* **96**, 330–345 (2016). <https://doi.org/10.1016/j.ijheatmasstransfer.2016.01.024>
21. T. Zhou, C. Peng, Z. Wang et al., Application of grey model on analyzing the passive natural circulation residual heat removal system of HTR-10. *Nucl. Sci. Tech.* **19**, 308–313 (2008). [https://doi.org/10.1016/S1001-8042\(09\)60009-9](https://doi.org/10.1016/S1001-8042(09)60009-9)
22. S. Unger, E. Krepper, M. Beyer et al., Numerical optimization of a finned tube bundle heat exchanger arrangement for passive spent fuel pool cooling to ambient air. *Nucl. Eng. Des.* **361**, 110549 (2020). <https://doi.org/10.1016/j.nucengdes.2020.110549>
23. A. Kumar, J.B. Joshi, A.K. Nayak et al., 3D CFD simulations of air cooled condenser-III: thermal–hydraulic characteristics and design optimization under forced convection conditions. *Int. J. Heat Mass Transf.* **93**, 1227–1247 (2016). <https://doi.org/10.1016/j.ijheatmasstransfer.2015.10.048>
24. S. Unger, M. Beyer, J. Thiele et al., Experimental study of the natural convection heat transfer performance for finned oval tubes at different tube tilt angles. *Exp. Therm. Fluid Sci.* **105**, 100–108 (2019). <https://doi.org/10.1016/j.expthermflusci.2019.03.016>
25. S. Unger, M. Beyer, M. Arlit et al., An experimental investigation on the air-side heat transfer and flow resistance of finned short oval tubes at different tube tilt angles. *Int. J. Therm. Sci.* **140**, 225–237 (2019). <https://doi.org/10.1016/j.ijthermalsci.2019.02.045>
26. Z. Xiong, C. Ye, M. Wang et al., Experimental study on the sub-atmospheric loop heat pipe passive cooling system for spent fuel pool. *Prog. Nucl. Energy* **79**, 40–47 (2015). <https://doi.org/10.1016/j.anucene.2015.03.045>

27. Z. Xiong, H. Gu, M. Wang et al., The thermal performance of a loop-type heat pipe for passively removing residual heat from spent fuel pool. *Nucl. Eng. Des.* **280**, 262–268 (2014). <https://doi.org/10.1016/j.nucengdes.2014.09.022>
28. M. Wang, Y. Wang, W. Tian et al., Recent progress of CFD applications in PWR thermal hydraulics study and future directions. *Ann. Nucl. Energy* **150**, 107836 (2021). <https://doi.org/10.1016/j.anucene.2020.107836>
29. Z. Xiong, M. Wang, H. Gu et al., Experimental study on heat pipe heat removal capacity for passive cooling of spent fuel pool. *Ann. Nucl. Energy* **83**, 258–263 (2015). <https://doi.org/10.1016/j.anucene.2014.10.015>
30. W.-T. Li, X.-K. Meng, H.-Z. Bian et al., Numerical analysis of heat transfer enhancement on steam condensation in the presence of air outside the tube. *Nucl. Sci. Tech.* **33**, 100 (2022). <https://doi.org/10.1007/s41365-022-01090-2>
31. Z. Lai, *Air Cooled Heat Exchanger*. (China Petrochemical Press, 2010)
32. B. Launder, D.B. Spalding, The numerical computation of turbulent flow computer methods. *Comput. Method Appl. M.* **3**, 269–289 (1974). [https://doi.org/10.1016/0045-7825\(74\)90029-2](https://doi.org/10.1016/0045-7825(74)90029-2)
33. Y. Deng, *Numerical Simulation of Natural Convection Heat Transfer in Spent Fuel Pools and Structural Optimization*. Dissertation. (Shandong University; 2018) (in Chinese)
34. K. Qiao, H. Tao, Y. Li et al., Numerical study on long-term passive heat removal of EPRHR cooling water tank (CWT) using heat pipe heat exchanger. *Ann. Nucl. Energy* **175**, 109212 (2022). <https://doi.org/10.1016/j.anucene.2022.109212>
35. S. He, M. Wang, W. Tian et al., Development of an OpenFOAM solver for numerical simulations of shell-and-tube heat exchangers based on porous media model. *Appl. Therm. Eng.* **210**, 118389 (2022). <https://doi.org/10.1016/j.applthermaleng.2022.118389>
36. M. Wang, A. Manera, M.J. Memmott et al., Preliminary design of the I2S-LWR containment system. *Ann. Nucl. Energy* **145**, 106065 (2020). <https://doi.org/10.1016/j.anucene.2018.03.014>
37. W. Fu, X. Li, X. Wu et al., Investigation of a long term passive cooling system using two-phase thermosyphon loops for the nuclear reactor spent fuel pool. *Ann. Nucl. Energy* **85**, 346–356 (2015). <https://doi.org/10.1016/j.anucene.2015.05.026>
38. Z.-X. Gu, Q.-X. Zhang, Y. Gu et al., Verification of a self-developed CFD-based multi-physics coupled code MPC-LBE for LBE-cooled reactor. *Nucl. Sci. Tech.* **32**, 52 (2021). <https://doi.org/10.1007/s41365-021-00887-x>
39. Y. Wu, J. Cheng, H. Zhu et al., Experimental study on heat transfer characteristics of separated heat pipe with compact structure for spent fuel pool. *Ann. Nucl. Energy* **181**, 109580 (2023). <https://doi.org/10.1016/j.anucene.2022.109580>
40. Q. Li, H. Li, X. Dong et al., Evaluation of wind energy in Weihai City of Shandong Province based on numerical simulation. *J. Anhui Agric. Sci.* **40**(1), 457–463 (2012). (in Chinese)
41. P. Wang, J. Cheng, F. Yuan et al., Application of time-series model on the temperature variation analysis in Weihai in recent 50 years. *South-to-North Water Transf. Water Sci.* **13**, 1051–1055 (2015). (in Chinese)

Publisher's Note Springer Nature remains neutral with regard to jurisdictional claims in published maps and institutional affiliations.

Springer Nature or its licensor (e.g. a society or other partner) holds exclusive rights to this article under a publishing agreement with the author(s) or other rightsholder(s); author self-archiving of the accepted manuscript version of this article is solely governed by the terms of such publishing agreement and applicable law.